

**This item is the archived peer-reviewed author-version of:**

A sensing integrated DFT-spread OFDM system for Terahertz communications

**Reference:**

Wu Yongzhi, Lemic Filip, Han Chong, Chen Zhi.- A sensing integrated DFT-spread OFDM system for Terahertz communications  
VTC ... : IEEE VTS ... vehicular technology conference- ISSN 1090-3038 - New york, IEEE, (2021)5 p.  
Full text (Publisher's DOI): <https://doi.org/10.1109/VTC2021-SPRING51267.2021.9448728>  
To cite this reference: <https://hdl.handle.net/10067/1816210151162165141>

# A Sensing Integrated DFT-Spread OFDM System for Terahertz Communications

Yongzhi Wu<sup>1</sup>, Filip Lemic<sup>2</sup>, Chong Han<sup>1</sup>, and Zhi Chen<sup>3</sup>

<sup>1</sup>Shanghai Jiao Tong University, China (email: {yongzhi.wu, chong.han}@sjtu.edu.cn)

<sup>2</sup>University of Antwerpen - imec, Belgium (email: filip.lemic@uantwerpen.be)

<sup>3</sup>University of Electronic Science and Technology of China, China (email: chenzhi@uestc.edu.cn)

**Abstract**—Terahertz (THz) communications are envisioned as a key technology of next-generation wireless systems due to its ultra-broad bandwidth. By integrating communication and sensing, the THz joint communication and sensing (JCS) system can realize both unprecedented data rates and ubiquitously accurate sensing. However, THz JCS meets stringent challenges due to the peculiarities of THz channel and devices. In this work, a sensing integrated discrete Fourier transform spread orthogonal frequency division multiplexing (SI-DFT-s-OFDM) system is proposed for THz JCS. The proposed system is able to provide lower peak-to-average power ratio than OFDM. Without compromising communication capabilities, SI-DFT-s-OFDM can realize millimeter-level range estimation accuracy and improve the velocity estimation accuracy by 10 times than OFDM. Finally, SI-DFT-s-OFDM achieves 18% improvement of data rate over DFT-s-OFDM.

## I. INTRODUCTION

Recently, the exhaustion of spectrum resources in the microwave band has motivated the adoption of the Terahertz (THz) band (0.1-10 THz). World Radiocommunication Conference 2019 (WRC-19) has identified 275-450 GHz for the land mobile and fixed services applications [1]. On one hand, the ultra-broad bandwidth in the THz band enables ultra-fast data rate and ultra-high sensing accuracy. On the other hand, with the non-ionization of THz radiation that is safe to human body, small size of THz antennas is able to support highly portable and wearable devices.

With the trend of moving up the carrier frequencies, the sixth-generation (6G) wireless communication systems envisages integrating communication and sensing to achieve a promising blueprint, i.e., all things sensing, connected, intelligent [2]. Integration of communication and sensing can enhance the spectrum efficiency, reduce the hardware cost and share information across communication and sensing modules. To further realize Tbps communication and millimeter-level sensing accuracy, the THz joint communication and sensing (JCS) is envisioned to guarantee high quality-of-experience (QoE) for various services and applications, such as autonomous driving in vehicles networks, wireless virtual reality (VR) communication and sensing, and THz Internet-of-Things (Tera-IoT) [3]. In addition, THz JCS provides various sensing services, including sensing, localization, imaging and spectrogram [3].

Despite the great promise of THz JCS techniques, stringent challenges are encountered as a result of the distinctive features of THz wave propagation and devices. First, since the free space propagation loss and reflection loss become stronger

in the THz band, the number of dominant rays for a communication link is reduced [4]. The directional antennas are used to provide high antenna gains and compensate for the severe path loss, which increases the coherence bandwidth of the communication channel [5]. However, this phenomenon is not entirely applicable to the sensing channel, which needs to be considered when designing a THz JCS waveform. Second, the power amplifier (PA) efficiency of transmitters at higher frequencies is more sensitive to the peak-to-average power ratio (PAPR) of the transmit signal. Lower PAPR should be taken into account to promote efficient THz JCS. Orthogonal frequency division multiplexing (OFDM) based JCS, which is spectrum-efficient and realizes good sensing accuracy, has been studied [6]–[8]. However, OFDM suffers from a high PAPR [9] and may not be applicable for THz systems. By contrast, single-carrier approaches [7], [10] realize range estimation by using the coded sequence with good auto-correlation property, which nevertheless sacrifice data rates drastically.

In this paper, we propose a sensing integrated discrete Fourier transform spread OFDM (SI-DFT-s-OFDM) waveform, which maintains the single-carrier characteristic and provide lower PAPR. The main contributions of our work include:

- We describe the key distinctions of the communication and sensing channels for THz JCS. **Motivated by this, we propose a novel SI-DFT-s-OFDM system**, which contains three types of transmission blocks with different cyclic prefix (CP) lengths. The proposed system utilizes the specific features of THz communication and sensing channels, and reduces the PAPR by more than 3 dB.
- **We propose a reference block based sensing (RBS) method at the sensing receiver for the SI-DFT-s-OFDM system.** Our simulations show that the proposed method can realize millimeter-level accuracy for range estimation and improve the velocity estimation accuracy by 10 times compared to the data block based sensing (DBS) of OFDM.
- **We provide a frequency domain equalization (FDE) method at the communication receiver.** The simulations indicate that the proposed system can reach 2.2 Gbps data rate with 1.28 GHz bandwidth and achieves 18% improvement of data rate over DFT-s-OFDM with only reference blocks.

The structure of this paper is organized as follows. The system model and the proposed SI-DFT-s-OFDM for THz JCS

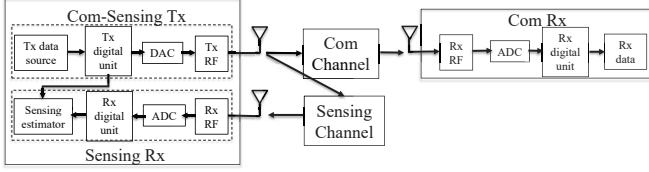


Fig. 1. System model for THz joint communication and sensing.

are respectively presented in Sec. II and Sec. III. A sensing algorithm and a FDE method are provided in Sec. IV and Sec. V. In Sec. VI, the simulation results are carried out. Finally, the paper is concluded in Sec. VII.

## II. SYSTEM MODEL

### A. Basic System Framework

As illustrated in Fig. 1, the transmitter (Tx) side of the THz-JCS system is composed of four components, including Tx data source, Tx digital, digital-to-analog converter (DAC), and Tx radio frequency (RF). The output signal of the Tx serves for both communication and sensing functionalities simultaneously, which is regarded as a joint communication-sensing transmitter (Com-Sensing Tx). Then the Tx signal propagates either through the communication channel to the communication receiver (Com Rx), and through the sensing channel to the sensing receiver (Sensing Rx).

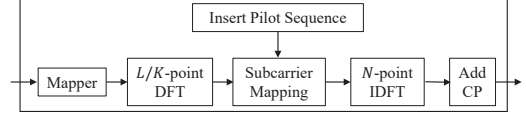
The Com Rx consists of Rx radio frequency (RF), analog-to-digital converter (ADC), and Rx digital unit, the operations of which are inverse to the Com-Sensing Tx. The Sensing Rx conducts similar operations on the received signal from the sensing channel, except that the output of the Rx digital unit feeds to the sensing estimator. The detailed operations of the digital units are presented in the subsequent subsections.

### B. Channel Model

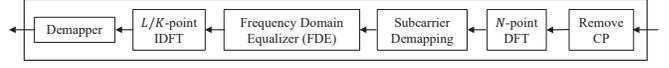
We formulate the channel models for THz JCS with a  $(N_r + 1)$ -ray communication channel model and a  $P$ -target sensing channel model, respectively as follows. On one hand, the channel impulse response (CIR) of the  $(N_r + 1)$ -ray communication channel is [5]

$$h_c(t, \tau) = \alpha_{\text{LoS}} e^{j2\pi\nu_{\text{LoS}}t} \delta(\tau - \tau_{\text{LoS}}) + \sum_{i=1}^{N_r} \alpha_{\text{NLoS}}^{(i)} e^{j2\pi\nu_{\text{NLoS}}^{(i)}t} \delta(\tau - \tau_{\text{NLoS}}^{(i)}) \quad (1)$$

where  $\delta(\cdot)$  denotes the Dirac delta function,  $\alpha_{\text{LoS}}$  and  $\alpha_{\text{NLoS}}^{(i)}$  represent the attenuation for the LoS ray and  $i^{\text{th}}$  NLoS ray, respectively.  $N_r$  describes the number of NLoS rays. The propagation delay  $\tau_{\text{LoS}}$  for the LoS ray and  $\tau_{\text{NLoS}}^{(i)}$  for the  $i^{\text{th}}$  NLoS ray can be computed by the equations  $\tau_{\text{LoS}} = \frac{r_{\text{LoS}}}{c_0}$  and  $\tau_{\text{NLoS}}^{(i)} = \frac{r_{\text{NLoS}}^{(i)}}{c_0}$ , where  $r_{\text{LoS}}$  and  $r_{\text{NLoS}}^{(i)}$  stand for the LoS path distance and the  $i^{\text{th}}$  NLoS path distance, and  $c_0$  is the speed of the light. Meanwhile, the time-varying channel response  $h_c(t, \tau)$  is influenced by the Doppler shift  $\nu_{\text{LoS}}$  along the LoS path and  $\nu_{\text{NLoS}}^{(i)}$  along the  $i^{\text{th}}$  NLoS path, which are calculated by  $\nu = \frac{f_c v}{c_0}$ , where  $v$  represents the relative speed between the



(a) The structure of the Tx digital unit.



(b) The structure of the Rx digital unit.

Fig. 2. The structures of the digital units for the sensing DFT-spread OFDM.

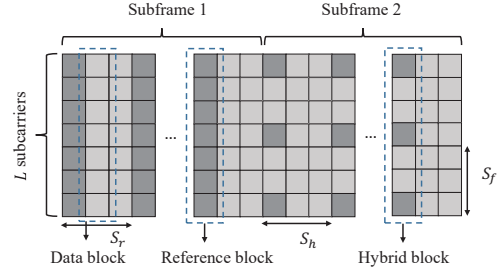


Fig. 3. Frame structure of SI-DFT-s-OFDM systems.

Tx and the Com Rx along the corresponding path. On the other hand, the CIR  $P$ -target sensing channel is described as

$$h_s(t, \tau) = \sum_{p=1}^P \alpha_p e^{j2\pi\nu_p t} \delta(\tau - \tau_p) \quad (2)$$

where  $P$  is the number of the considered targets, each of which corresponds to one back-reflected path with the attenuation  $\alpha_p$ . Due to the two-way propagation, the delay and the Doppler shift are calculated by  $\tau_p = \frac{2r_p}{c_0}$  and  $\nu_p = \frac{2f_c v_p}{c_0}$ , where  $r_p$  and  $v_p$  stand for the range and relative speed of the  $p^{\text{th}}$  target.

When it comes to the THz band, by decreasing the beamwidth towards the Com Rx, the number of significant multi-ray components decreases and the delay spread of the communication channel is reduced. However, as the sensing targets are independently and randomly distributed around the transmitter, their distances and speeds can be very different. Thus, the delay spread of sensing channel can be much larger than that of communication channel in the THz band. As a result, different CP lengths and pilot types are required for communication and sensing in the waveform design.

## III. SENSING INTEGRATED DFT-SPREAD OFDM

### A. Tx Digital Unit

The structure of the Tx digital unit in the sensing DFT-spread OFDM system is illustrated in Fig. 2(a). At the transmitter, the transmitted data is grouped into multiple data frames. Each data frame with  $M$  blocks consists of  $M_{\text{DB}}$  data blocks,  $M_{\text{RB}}$  reference blocks and  $M_{\text{HB}}$  hybrid blocks. The input bit streams are firstly mapped to the data sequences with the  $Q$ -ary quadrature amplitude modulation (QAM). The modulated symbols are grouped into the data blocks  $\tilde{\mathbf{x}}_{D_m} = [\tilde{x}_{m,0}, \tilde{x}_{m,1}, \dots, \tilde{x}_{m,L-1}]^T$ ,  $m = 0, 1, \dots, M_{\text{DB}} - 1$ ,

each containing  $L$  symbols, and the hybrid blocks  $\mathbf{u}_{H_m} = [u_{m,0}, u_{m,1}, \dots, u_{m,K-1}]^T, m = 0, 1, \dots, M_{HB} - 1$ , each containing  $K$  symbols. Then a  $L$ -point DFT is performed on  $\tilde{\mathbf{x}}_{D_m}$  and produces a frequency domain representation

$$\tilde{\mathbf{X}}_{D_m} = \mathbf{W}_L \tilde{\mathbf{x}}_{D_m}, m = 0, 1, \dots, M_{DB} - 1 \quad (3)$$

where  $\tilde{\mathbf{X}}_{D_m} \triangleq [\tilde{X}_{m,0}, \tilde{X}_{m,1}, \dots, \tilde{X}_{m,L-1}]^T \in \mathbb{C}^{L \times 1}$ , and  $\mathbf{W}_L \in \mathbb{C}^{L \times L}$  denotes the DFT matrix with the size  $L$ ,  $\mathbf{W}_L(m, n) \triangleq \frac{1}{\sqrt{L}} \exp(-j2\pi mn/L), m, n = 0, 1, \dots, L - 1$ . Meanwhile, a  $K$ -point DFT is performed on  $\mathbf{u}_{H_m}$  and produces a frequency domain representation

$$\tilde{\mathbf{U}}_{H_m} = \mathbf{W}_K \mathbf{u}_{H_m}, m = 0, 1, \dots, M_{HB} - 1 \quad (4)$$

where  $\tilde{\mathbf{U}}_{H_m} \triangleq [\tilde{U}_{m,0}, \tilde{U}_{m,1}, \dots, \tilde{U}_{m,K-1}]^T \in \mathbb{C}^{K \times 1}$ , and  $\mathbf{W}_K \in \mathbb{C}^{K \times K}$  refers to the DFT matrix with size  $K$ ,  $\mathbf{W}_K(m, n) \triangleq \frac{1}{\sqrt{K}} \exp(-j2\pi mn/K), m, n = 0, 1, \dots, K - 1$ . Then the constant enveloped Zadoff-Chu (ZC) sequence with the size  $K_p = L - K$ ,  $\mathbf{S}_{H_m} = [S_{m,0}, S_{m,1}, \dots, S_{m,K_p-1}]^T$ , is inserted into  $\tilde{\mathbf{U}}_{H_m}$  with equi-distance  $S_f = L/K_p$  and the length of the hybrid blocks is filled to  $L$ ,  $\mathbf{U}_{H_m} = [U_{m,0}, U_{m,1}, \dots, U_{m,L-1}]^T$ , where

$$U_{m,l} = \begin{cases} S_{m,l/S_f}, l = S_f \cdot k, k = 0, 1, \dots, K_p - 1 \\ \tilde{U}_{m,l-r}, r = \lceil l/S_f \rceil, \text{ otherwise} \end{cases} \quad (5)$$

In addition, the ZC sequence with a size  $L$ , i.e.,  $\mathbf{P}_{R_m} = [P_{m,0}, P_{m,1}, \dots, P_{m,L-1}]^T, m = 0, 1, \dots, M_{RB} - 1$ , is used for the reference blocks.

In a data frame of the frequency domain signal, the reference blocks and the hybrid blocks are inserted into the data blocks with equi-distance  $S_r$  and  $S_h$ , respectively. Thus, the frequency domain SI-DFT-s-OFDM signal is given by

$$\mathbf{X}_m = \begin{cases} \mathbf{P}_{R_q}, m = S_r \cdot q, q = 0, 1, \dots, M_{RB} - 1 \\ \mathbf{U}_{H_q}, m = S_h \cdot q + S_r \cdot M_{RB}, q = 0, 1, \dots, M_{HB} - 1 \\ \tilde{\mathbf{X}}_{D_q}, q = m - q_m, \text{ otherwise} \end{cases} \quad (6)$$

where  $\mathbf{X}_m \triangleq [X_{m,0}, X_{m,1}, \dots, X_{m,L-1}]^T \in \mathbb{C}^{L \times 1}, m = 0, 1, \dots, M - 1$ , and  $q_m$  represents the number of reference blocks and hybrid blocks before  $m^{\text{th}}$  block in a frame. The frame structure of the SI-DFT-s-OFDM is illustrated in Fig. 3. Essentially, a data frame can be divided into two subframes, subframe 1 with  $M_{RB}$  reference blocks and  $(S_r - 1)M_{RB}$  data blocks, and subframe 2 with  $M_{HB}$  hybrid blocks and  $(S_h - 1)M_{HB}$  data blocks.

Next, the subcarrier mapping assigns each block to a set of  $L$  consecutive subcarriers and inserts zeros into other  $(N - L)$  unused subcarriers. Then the  $m^{\text{th}}$  time domain SI-DFT-s-OFDM block,  $\mathbf{x}_m = [x_{m,0}, x_{m,1}, \dots, x_{m,N-1}]^T$ , is generated by performing an  $N$ -point IDFT,

$$\mathbf{x}_m = \mathbf{D}_N \begin{bmatrix} \mathbf{X}_m \\ \mathbf{0}_{(N-L) \times 1} \end{bmatrix} \quad (7)$$

where  $\mathbf{D}_N \in \mathbb{C}^{N \times N}$  refers to the IDFT matrix with size  $N$ ,  $\mathbf{D}_N(m, n) = \frac{1}{\sqrt{L}} \exp(j2\pi mn/N), m, n = 0, 1, \dots, N - 1$ . The subcarrier spacing is denoted by  $\Delta f$ .

In order to avoid the inter-block interference, a cyclic prefix (CP) part is added as a guard interval between adjacent blocks. The CP length for the reference blocks is  $N_{RB}$  and the CP length for other blocks is  $N_{cp}$ . Then the total symbol durations of the reference block and other blocks are respectively given by  $T_{RB} = (1 + \frac{N_{RB}}{N})T$  and  $T_{DB} = (1 + \frac{N_{cp}}{N})T$ , where  $T = \frac{1}{\Delta f}$  is the original symbol duration.

## B. Rx Digital Unit

In Fig. 2(b), at the Rx side, after the OFDM demodulation including removing CP,  $N$ -point DFT operation and subcarrier demapping, the frequency domain received signals,  $\mathbf{Y}_m = [Y_{m,0}, Y_{m,1}, \dots, Y_{m,L-1}]^T$ , are given by

$$\mathbf{Y}_m = \mathbf{H}_m \mathbf{X}_m + \mathbf{Z}_m, m = 0, 1, \dots, M - 1 \quad (8)$$

where  $\mathbf{H}_m \triangleq \text{diag}(H_{m,0}, H_{m,1}, \dots, H_{m,L-1})$  is an  $L \times L$  diagonal matrix that denotes the channel frequency response (CFR), and  $\mathbf{Z}_m \triangleq [Z_{m,0}, Z_{m,1}, \dots, Z_{m,L-1}]^T$  refers to the additive white Gaussian noise (AWGN). Next, the communication receiver estimates the CFR by employing the pilot sequences in the reference blocks and the hybrid blocks. Then the FDE is performed to estimate  $\tilde{\mathbf{X}}_{D_m}$  and  $\mathbf{U}_{H_m}$ . Finally, the  $L$ -point and  $K$ -point IDFTs are performed on the estimated data blocks and the hybrid blocks, the output of which goes into the demapper and is detected as the information bit streams.

## IV. SENSING ALGORITHM

### A. Data Block Based Sensing Algorithm

First, we introduce the data block based sensing algorithm in the OFDM system. In this case, only the data blocks are considered, then the frequency domain signals at the sensing receiver can be expressed as

$$\tilde{Y}_{m,n}^{(s)} = H_{m,n}^{(s)} \tilde{X}_{m,n} + Z_{m,n}^{(s)}, \quad m = 0, 1, \dots, M_{DB} - 1; n = 0, 1, \dots, L - 1 \quad (9)$$

where  $H_{m,n}^{(s)}$  denotes the sensing CFR at the data blocks and  $Z_{m,n}^{(s)}$  refers to the AWGN in the sensing channel. With the above received blocks and the transmitted data blocks, we can directly estimate the CFR, which contains the delay and Doppler information of the sensing channel, by simply using the least square (LS) channel estimation,

$$\hat{H}_{m,n}^{(s)} = \frac{\tilde{Y}_{m,n}^{(s)}}{\tilde{X}_{m,n}} = H_{m,n}^{(s)} + \frac{Z_{m,n}^{(s)}}{\tilde{X}_{m,n}} \quad (10)$$

Then the range and the velocity of the targets can be extracted by different sensing algorithms, such as maximum likelihood estimation (MLE) and multiple signal classification (MUSIC).

However, the data block based sensing algorithm does not work for the DFT-s-OFDM system, since the amplitudes of  $\tilde{X}_{m,n}$  vary a lot for different  $m$  and  $n$ , i.e.,  $\tilde{X}_{m,n}$  is very small in some cases, which causes the noise enhancement and bad channel estimation. Thus, the sensing accuracy of this method for DFT-s-OFDM is much worse than that for OFDM.

## B. Reference Block Based Sensing Algorithm

The reference blocks are usually regarded as the demodulation reference signal (DMRS) and generated from ZC sequences, which have a constant envelope and good PAPR performance. Thanks to the very short symbol duration of THz waveform, a number of reference blocks can be inserted into a data frame, which contributes to high sensing accuracy. We propose the reference block based sensing algorithm as follows.

The received reference signals at the sensing receiver are

$$\tilde{P}_{m,n}^{(s)} = H_{m,n}^{(s)} P_{m,n} + Z_{m,n}^{(s)} \quad (11)$$

where  $m = 0, 1, \dots, M_{\text{RB}} - 1$ , and  $n = 0, 1, \dots, L - 1$ . The sensing CFR at the reference blocks is given by

$$H_{m,n}^{(s)} = \sum_{p=1}^P \alpha_p e^{j\varphi_p} e^{j2\pi\nu_p m (T_{\text{RB}} + (S_r - 1)T_{\text{DB}})} e^{-j2\pi\tau_p n \Delta f} \quad (12)$$

Due to the constant envelope of the reference blocks, the LS estimator does not introduce additional estimation error caused by the amplitude variation of pilot signal. Then we can calculate the time-frequency correlation function of the CFR as

$$\begin{aligned} R_H(\Delta m, \Delta n) &= E \left\{ \hat{H}_{m-\Delta m, n}^{(s)*} \hat{H}_{m, n+\Delta n}^{(s)} \right\} \\ &= \sum_{p=1}^P |\alpha_p|^2 e^{j2\pi\nu_p \Delta m (T_{\text{RB}} + (S_r - 1)T_{\text{DB}})} e^{-j2\pi\tau_p \Delta n \Delta f} \\ &\quad + \sigma_z^2 \delta(\Delta m, \Delta n), \end{aligned} \quad (13)$$

where  $\sigma_z^2$  refers to the noise power. Furthermore, the range and velocity can be jointly estimated from this time-frequency correlation function by using the two-dimensional (2D) subspace-based methods, such as 2D MUSIC.

By using the reference block based sensing algorithm, the maximum unambiguous range and the range resolution are computed by  $r_{\text{max}} = \frac{c_0}{2\Delta f}$ ,  $\Delta r = \frac{c_0}{2L\Delta f}$ , which are the same as those of the OFDM system. The maximum unambiguous velocity and the velocity resolution are computed by

$$\begin{aligned} v_{\text{max}} &= \frac{c_0}{2f_c (T_{\text{RB}} + (S_r - 1)T_{\text{DB}})}, \\ \Delta v &= \frac{c_0}{2M_{\text{RB}} f_c (T_{\text{RB}} + (S_r - 1)T_{\text{DB}})} \end{aligned} \quad (14)$$

While the maximum unambiguous velocity of the RBS is less than that of the DBS in the OFDM system, which equals to  $\frac{c_0}{2f_c T_{\text{RB}}}$ , it does not affect the sensing performance of the velocity estimation, since the speed of the realistic moving objects is much slower than  $v_{\text{max}}$ . Meanwhile, the RBS achieves higher velocity resolution, which depends on the period of the reference block in time.

## V. FREQUENCY DOMAIN EQUALIZATION

The reference blocks are not only used for the sensing estimation at the sensing receiver but also for the frequency domain equalization at the communication receiver. In order to reduce the overhead of the pilot sequence, the hybrid blocks are added to replace the reference blocks in the subframe 2.

However, if we use the hybrid blocks to estimate the target range, the maximum unambiguous range is only  $\frac{1}{S_f}$  of the RBS, which is not able to support long-range sensing. In this section, we propose a frequency domain equalization method of subframe 1 and subframe 2.

### A. Channel Estimation for Subframe 1

In subframe 1, the block type of pilot arrangement satisfies that the time domain period of reference block is much smaller than the coherence time of the communication channel. In this case, we use a 1D linear channel interpolation method to estimate the CFR at the data blocks of subframe 1,

$$\begin{aligned} \hat{H}_{m,n} &= \frac{T_{\text{RB}} + (m - kS_r - 1)T_{\text{DB}}}{T_{\text{RB}} + (S_r - 1)T_{\text{DB}}} \left( \hat{H}_{(k+1)S_r, n} - \hat{H}_{kS_r, n} \right) \\ &\quad + \hat{H}_{kS_r, n}, \quad kS_r < m < (k+1)S_r, \quad k = 0, 1, \dots, M_{\text{RB}} - 1 \end{aligned} \quad (15)$$

where  $\hat{H}_{kS_r, n}$  represents the estimated CFR at the  $k^{\text{th}}$  reference block and the  $n^{\text{th}}$  subcarrier, obtained from the LS estimation.

### B. Channel Estimation for Subframe 2

In subframe 2, the periods of pilot symbols in time and frequency should be much smaller than the coherence time and the coherence bandwidth of the communication channel, respectively. We propose a two-stage channel estimation method for this 2D grid-type pilot arrangement.

At the first stage, we estimate the CFR at the hybrid blocks with the DFT-based channel estimation. First, we conduct the 1D linear channel interpolation method along the frequency dimension to obtain the estimated CFR at the data symbols from the CFR at the pilot symbols in each hybrid block,

$$\begin{aligned} \hat{H}_m[n] &= \hat{H}_{M_{\text{RB}}S_r + mS_h, lS_f} + \frac{n - lS_f}{S_f} \\ &\quad \cdot \left( \hat{H}_{M_{\text{RB}}S_r + mS_h, (l+1)S_f} - \hat{H}_{M_{\text{RB}}S_r + mS_h, lS_f} \right), \\ &\quad lS_f < n < (l+1)S_f, \quad l = 0, 1, \dots, K_p - 1, \end{aligned} \quad (16)$$

where  $\hat{H}_{M_{\text{RB}}S_r + mS_h, lS_f}$  refers to the estimated CFR at the  $l^{\text{th}}$  pilot symbol of the  $m^{\text{th}}$  hybrid block. By taking the IDFT of  $\hat{\mathbf{H}}_m \triangleq [\hat{H}_m[0], \hat{H}_m[1], \dots, \hat{H}_m[L-1]]^T$ , we obtain

$$\hat{\mathbf{h}}_m = \mathbf{D}_L \hat{\mathbf{H}}_m \quad (17)$$

Suppose that the maximum excess delay of the communication channel is  $N_\tau$ . We only consider the first  $N_\tau$  channel coefficients and transform them back to the frequency domain,

$$\hat{\mathbf{H}}_{m, \text{DFT}} = \mathbf{W}_L \begin{bmatrix} \mathbf{I}_{N_\tau} & \mathbf{0}_{N_\tau \times (L - N_\tau)} \\ \mathbf{0}_{(L - N_\tau) \times N_\tau} & \mathbf{0}_{(L - N_\tau) \times (L - N_\tau)} \end{bmatrix} \hat{\mathbf{h}}_m \quad (18)$$

By ignoring the last  $(L - N_\tau)$  channel coefficients that contain the noise only, the performance of the channel estimation for the hybrid blocks can be improved.

At the second stage, the CFR at the data blocks of the subframe 2 can be estimated by using the 1D linear interpolation along the time dimension based on the CFRs at the hybrid blocks. Finally, the estimated CFRs can be used to equalize the received data signals.

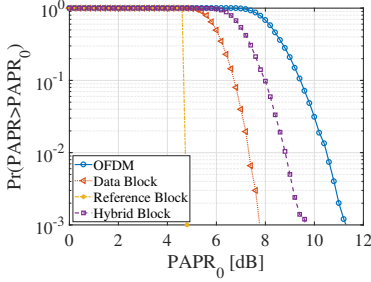


Fig. 4. Comparison of PAPR between OFDM and different blocks of SI-DFT-s-OFDM.

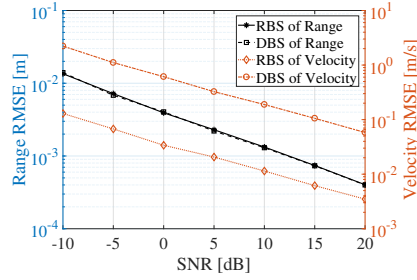


Fig. 5. RMSE of range and velocity estimation using RBS of SI-DFT-s-OFDM and DBS of OFDM.

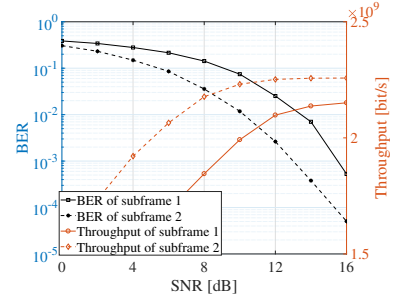


Fig. 6. BER and throughput of subframe 1 and subframe 2 in the SI-DFT-s-OFDM frame.

## VI. SIMULATION RESULTS

In this section, we provide the simulation results to illustrate the performance of the proposed SI-DFT-s-OFDM system as compared with the OFDM based JCS system. The key parameters include frequency at 0.3 THz, subcarrier spacing of 5 MHz, 256 subcarriers, block size of 256 and 4-QAM modulation. In this case, the maximum unambiguous range is 30 m and we can conduct Fast Fourier transform to reduce computational cost.

In Fig. 4, we evaluate the PAPR of the SI-DFT-s-OFDM and the OFDM baseband signals. The performance metric is the complementary cumulative distribution function (CCDF) of PAPR, i.e.,  $\Pr(\text{PAPR} > \text{PAPR}_0)$ . In order to make the discrete-time signal have the same PAPR as the continuous-time signal, we use 4-times oversampling. The pilot period in each hybrid block  $S_f$  equals to 8. We can observe that hybrid block has larger PAPR than data block and reference block, which are all lower than that of OFDM data block. In particular, the PAPR value of SI-DFT-s-OFDM data block is approximately 3.2 dB lower than OFDM at the CCDF of 1%.

In our simulations, the range and velocity of the reference target are 20 m and 10 m/s, respectively. We use 64 subcarriers and 32 reference blocks to reduce the computational cost. The CP duration of the reference block and the data block is set to  $T$  and  $\frac{1}{8}T$ . In Fig. 5, we compare the root mean square error (RMSE) of range and velocity estimation between the RBS of SI-DFT-s-OFDM and the DBS of OFDM. We learn that the accuracy of range estimation of the THz SI-DFT-s-OFDM system achieves  $10^{-3}$  m at SNR of 5 dB, which is similar to THz OFDM. Compared to the DBS, the accuracy of velocity estimation is improved by 10 times by using the RBS, which realizes  $10^{-2}$  m/s at SNR of 15 dB.

We consider a 3-ray THz simulated channel with the path distance [20, 23, 26] m, the relative speed [20, 15, 13] m/s and the normalized path power [0, -10, -10] dB to evaluate the bit error ratio (BER) and the throughput of SI-DFT-s-OFDM. The pilot period is set as  $S_r = 32, S_h = 32, S_f = 4$ . By employing the proposed two-stage CE method, the BER of subframe 1 is lower than subframe 2. In addition, by developing a hybrid block design, we reduce the pilot overhead in subframe 2, the throughput of which is 18% higher than that of DFT-s-OFDM with only block type pilot at SNR of 8 dB.

## VII. CONCLUSION

In this paper, we propose a sensing integrated DFT-s-OFDM system for THz communications. We design a data frame for THz JCS, which utilizes the specific feature of THz communication and sensing channels. Furthermore, we provide a reference block based sensing algorithm for range and velocity estimation at the sensing receiver and a FDE method at the communication receiver. We demonstrate that the proposed SI-DFT-s-OFDM is able to reduce the PAPR, achieve higher data rate and realize a millimeter-level accuracy of range estimation.

### ACKNOWLEDGMENT

Chong Han acknowledges the support from the National Natural Science Foundation of China (NSFC) under Grant 62027806. Filip Lemic acknowledges the support from the European Commission (EU MSCA-IF-2019, nr. 893760) and Research Foundation - Flanders (FWO, nr. V406320N).

### REFERENCES

- [1] WRC-19, "World radiocommunication conference 2019 (wrc-19) final acts." [Online]. Available: [https://www.itu.int/dms\\_pub/itu-r/opb/act/R-ACT-WRC.14-2019-PDF-E.pdf](https://www.itu.int/dms_pub/itu-r/opb/act/R-ACT-WRC.14-2019-PDF-E.pdf)
- [2] Z. Zhang *et al.*, "6g wireless networks: Vision, requirements, architecture, and key technologies," *IEEE Veh. Technol. Mag.*, vol. 14, no. 3, pp. 28–41, 2019.
- [3] H. Saeeddeeen *et al.*, "Next generation terahertz communications: A rendezvous of sensing, imaging, and localization," *IEEE Commun. Mag.*, vol. 58, no. 5, pp. 69–75, 2020.
- [4] Y. Wu *et al.*, "Interference and coverage analysis for terahertz networks with indoor blockage effects and line-of-sight access point association," *to appear in IEEE Trans. Wireless Commun.*, 2020.
- [5] C. Han *et al.*, "Multi-ray channel modeling and wideband characterization for wireless communications in the terahertz band," *IEEE Trans. Wireless Commun.*, vol. 14, no. 5, pp. 2402–2412, May 2015.
- [6] C. R. Berger *et al.*, "Signal processing for passive radar using ofdm waveforms," *IEEE J. Sel. Topics Signal Process.*, vol. 4, no. 1, pp. 226–238, 2010.
- [7] C. Sturm *et al.*, "Waveform design and signal processing aspects for fusion of wireless communications and radar sensing," *Proc. IEEE*, vol. 99, no. 7, pp. 1236–1259, July 2011.
- [8] J. A. Zhang *et al.*, "Multibeam for joint communication and radar sensing using steerable analog antenna arrays," *IEEE Trans. Veh. Technol.*, vol. 68, no. 1, pp. 671–685, January 2019.
- [9] A. Sahin *et al.*, "Flexible dft-s-ofdm: Solutions and challenges," *IEEE Commun. Mag.*, vol. 54, no. 11, pp. 106–112, 2016.
- [10] P. Kumari *et al.*, "Ieee 802.11ad-based radar: An approach to joint vehicular communication-radar system," *IEEE Trans. Veh. Technol.*, vol. 67, no. 4, pp. 3012–3027, 2018.